

Estimation of Wind Conditions Utilizing RC Helicopter Dynamics

Anil Kumar , Member, IEEE, and Pinhas Ben-Tzvi , Senior Member, IEEE

Abstract—This paper investigates the applicability of a remote-controlled (RC) helicopter as a sensing platform for measuring local wind conditions. A simplified nonlinear multibody helicopter dynamics model has been proposed in this paper, which models local wind conditions in addition to capturing essential helicopter states such as fuselage dynamics, rotor inflow, blade flapping, and lead lagging. The critical aerodynamic parameters for the model were extracted using indoor calibration flights. This paper also presents the performance of particle swarm optimization in optimizing and validating the helicopter’s dynamic model parameters. An in-house developed multisensor instrumentation system was used to track the helicopter dynamics and extract wind model parameters through anomalies in the helicopter dynamics estimates. A three-dimensional (3-D) map of local wind conditions was generated for a controlled turbulent wind environment created in an indoor test facility. To validate the system’s performance, wind parameters estimated from the proposed system were quantitatively compared against the experimentally generated 3-D wind map.

Index Terms—Active particle filter (APF), particle swarm optimization (PSO), remote controlled (RC) helicopter dynamics, ship air wake, wind turbulence, wind-aircraft interaction.

NOMENCLATURE

$[\theta, \varphi, \psi]$	Pitch, roll, yaw angles of helicopter fuselage.
$[u, v, w]$	Linear velocity of helicopter fuselage.
$[p, q, r]$	Angular rates of helicopter fuselage.
$\delta_0, (\delta_c, \delta_s), \delta_T$	Commanded collective main rotor, cyclic main rotor, and tail rotor pitch angles.
$\theta_0, (\theta_c, \theta_s), \theta_T$	Instantaneous collective main rotor, cyclic main rotor, and tail rotor pitch angles.

Manuscript received January 31, 2018; revised June 27, 2018, September 27, 2018, February 11, 2019, and June 18, 2019; accepted July 28, 2019. Date of publication August 27, 2019; date of current version October 15, 2019. Recommended by Technical Editor T. Zhang. This work was supported in part by the Office of Naval Research Program Officer: Mr. John Kinzer (Code 351). (Corresponding author: Pinhas Ben-Tzvi.)

A. Kumar was with the Mechanical Engineering Department, Virginia Tech Blacksburg, VA 24060 USA. He is currently with the GM Cruise LLC, San Francisco, CA 94103 USA (e-mail: anilks@vt.edu).

P. Ben-Tzvi is with the Mechanical Engineering Department, Virginia Tech, Blacksburg, VA 24061 USA (e-mail: bentzvi@vt.edu).

Color versions of one or more of the figures in this article are available online at <http://ieeexplore.ieee.org>.

Digital Object Identifier 10.1109/TMECH.2019.2937844

$[\beta_0, \beta_c, \beta_s], [\zeta_0, \zeta_c, \zeta_s]$	Collective/cyclic main rotor blade flapping and lead-lag angles.
$[v_x, v_y, v_z], [\omega_x, \omega_y, \omega_z]$	Instantaneous mean external wind velocity vector and vorticity vector.
$[\lambda_0, \lambda_c], \chi$	Main rotor inflow wind flow field parameters and inflow incidence angles.
$[X, Y, Z], [L, M, N]$	Aerodynamic forces and moments in helicopter’s frame of reference.
$I_{xx}, I_{yy}, I_{zz}, I_{xz}$	Helicopter fuselage moment of inertia.
M_H	Helicopter fuselage mass.
R, R_T	Main rotor and tail rotor blade length.
Ω, Ω_T	Main rotor, and tail rotor speed.
C_T	Rotor thrust coefficient.
a_0	Lift curve slope.
g	Acceleration due to gravity.
γ, γ_f	Main rotor/flybar lock number.
$(-l_T, 0, h_T)$	Tail rotor coordinates.
$(0, 0, h_R)$	Main rotor hub coordinates.
$(-l_H, 0, 0)$	Horizontal fin coordinates.
K_β, K_ζ	Equivalent spring stiffness for rotor flapping and lead/lag motion.

I. INTRODUCTION

WIND turbulence plays a critical role in the operation of vertical takeoff and landing of aircrafts, such as helicopters, aboard naval vessels. Issues such as unsteady ship motion and limited deck area, when combined with the wind turbulence generated by the moving vessels (also known as ship air wakes), make the landing and takeoff of helicopters from naval platforms a very risky task. To mitigate such operational risks, safe “launch and recovery envelopes” are prescribed based on the class of the vessels in consideration [1]. Such safe flight envelopes are often determined with computational fluid dynamics (CFD) models and/or manual flight-testing. Significant research has been conducted to develop high-fidelity CFD models in order to predict the air wakes generated by moving vessels and their interaction with onboard aircraft [2]–[8]. Such models need experimental data for optimization and validation. Although most researchers perform wind tunnel testing to obtain experimental data for CFD model validation, very few researchers have conducted in situ measurements [9]–[11]. The scope of this paper is limited to in situ ship air wake measurement techniques.

Although the use of anemometers has been the most convenient means of air wake measurement [11]–[13], limitations such as high costs and extremely low spatial resolution have pushed researchers to explore airborne sensors. Mallon *et al.* [14] and Gamagedara *et al.* [15] have explored the use of airborne anemometers mounted on a quadrotor to map ship air wakes. This approach does overcome the spatial resolution issue with the anemometers, but requires extensive compensation for the anemometers' motion and, most importantly, the method is susceptible to the quadrotor's own rotor wakes. Volumetric anemometric sensors such as SoNAR detection and ranging (SoDAR)/LiGht detection and ranging (LiDARs) offer dense three-dimensional (3-D) wind measurements over large volumes. However, their bulky size and susceptibility to interference from nonatmospheric entities, restrict their usage to atmospheric wind profiling in the open (unlike ship air wakes that are close to ship structures) [16].

In recent approaches, researchers have attempted to explore the use of the dynamics of small unmanned aerial vehicles (UAVs) for the characterization of wind turbulence. Gonzalez-Rocha *et al.* in [17] demonstrated the use of a small quadrotor's motion to measure atmospheric winds through kinematic filtering. Their approach can also be applied to measure ship air wakes, but focuses only on the mean flow component of the ambient wind flow and ignores the effects of the UAV presence on the natural wind field. In addition, the lower value of the rotor disk area reduces the sensitivity of the UAV platform to wind turbulence. Similarly, Phelps *et al.* explored the use of the dynamics of instrumented fixed wing UAVs for mapping ship air wakes [18]. They flew the UAV in the lee of the superstructure of a cruising naval vessel and attempted to map ship air wake through deviations in the acceleration (from the aerodynamic lift/drag) of the aircraft. This approach can map air wakes in large volumes; however, the absence of hovering capabilities reduces the temporal resolution of the system.

In contrast to the other existing techniques for measuring ship air wakes, the proposed system uses RC helicopters for mapping ship air wakes. The hovering capabilities of the helicopter combined with its low cost and long operational range make it an ideal transducer to determine wind conditions. The large rotor disc area along with its low mass makes RC helicopters very sensitive to ship air wakes. The use of RC helicopters to map ship air wakes was first proposed by Metzger [19]; however, the approach ignored pilot-induced helicopter motion [20]. This concept was gradually extended by Kumar *et al.* in multiple iterations by modeling the contributions of pilot inputs in the helicopter's dynamics using machine learning [21]–[23]. In a recent approach, Kumar *et al.* modeled the rotational dynamics of an RC helicopter using neural networks and demonstrated a correlation between the helicopter dynamics and the temporal characteristics of a turbulent wind flow [16], [23]. However, machine learning is inherently a "black box" type modeling technique where the reliability of the output depends on the diversity of the training data and the complexity of the network topology (model).

To overcome this limitation, this paper presents a novel simplified nonlinear dynamic model-based approach to estimate

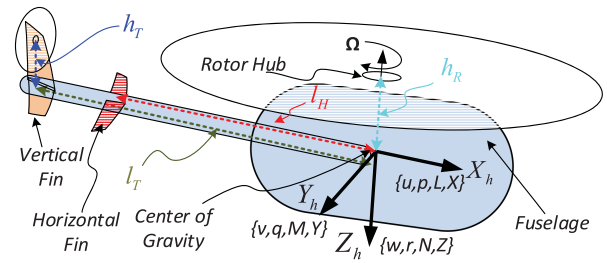


Fig. 1. Coordinate system for the proposed helicopter model.

ambient wind conditions (ship air wakes) using a flying RC helicopter. Also, the proposed approach overcomes the limitations of kinematic filtering [17], [18] by using a dynamics model based on particle filters. Active particle filters (APFs) have been selected over other traditional estimators such as extended Kalman filters (EKFs) in the proposed approach because of their unique capability of modeling non-Gaussian noise distribution in the system states and observations. With wind turbulence parameters being chaotic in nature, APFs suit well in this estimation problem.

The main contribution of this paper is modeling instantaneous aerodynamic interactions of an RC helicopter and using helicopter dynamics measurements with particle filter to estimate the ambient wind flow field. In contrast to the existing helicopter dynamics studies, which use popular spatially invariant control equivalent turbulence input (CETI) model [5], [6] for characterizing wind turbulence, the presented approach analytically estimates the aerodynamics of the RC helicopter in varying wind conditions (represented using localized wind flow models). The proposed system's capability to extract ship air wakes has been tested in an indoor calibration experiment where the helicopter was flown in artificially created wind turbulence.

II. HELICOPTER DYNAMICS AND AIR WAKES

This section describes the mathematical model used by the proposed system to capture the wind–helicopter interaction in the helicopter dynamics. The test platform being a lightweight RC helicopter permits the use of a simplified nonlinear model for its dynamics assuming the rotor blades and fuselage as rigid bodies. To simplify the modeling process, linear incompressible aerodynamics along with helicopter symmetry, a constant helicopter mass/inertia matrix, and rigid blades were assumed. Additionally, the Pitt–Peters linear static inflow model [24], (based on axial flow momentum theory) has been used to model helicopter-induced wind inflow. It has been assumed that the net wind field experienced by the helicopter body is an algebraic sum of the external wind flow field (air wakes) and the helicopter-induced inflow field. Also, because of near-hover/slow descent modes of operation, it has been assumed that the rotor wakes do not recirculate and affect the rotor inflow. Fig. 1 shows the frame of reference assignment on the helicopter for the purpose of dynamic modeling.

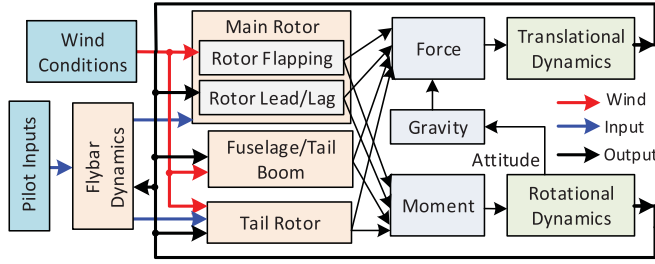


Fig. 2. Helicopter dynamics models and subsystems.

A. Nonlinear Helicopter Flight Dynamics Model

The proposed helicopter model incorporates critical dynamics components such as a two-blade articulated rotor, fuselage, flybar stabilizer, and tail rotor. The helicopter's nonlinear dynamics can be expressed as (1) shown at the bottom of this page, where \mathbf{x} is the dynamics state vector, \mathbf{w} is the local wind condition parameters, and \mathbf{u} is the pilot input vector. Here, \mathbf{B} represents the set of the helicopter body (fuselage) states consisting of translational velocity \mathbf{v}_H (u, v, w), roll-pitch-yaw attitude angle states (θ, φ, ψ) relative to the inertial northeast-Down frame of reference, and angular rates $\boldsymbol{\omega}_H$ along the roll-pitch-yaw axes (p, q, r). The sets \mathbf{F} , \mathbf{L} , \mathbf{I} , and \mathbf{P} represent dynamic states involving flapping angles, rotor lead-lag angles, stabilizer (flybar) seesaw flapping angles, and static rotor inflow field [24] and rotor blades pitch angles, respectively. The subscripts “0,” “c,” and “s” represent collective and two cyclic components of the various quantities when represented in a multiblade coordinate system [6], [25]. The pilot input \mathbf{u} consists of collective (δ_0), two cyclic (δ_c, δ_s) and tail (δ_T) rotor blade pitch angles [26].

Helicopters, being highly complex systems, feature nonlinear dynamics obtained from multiple interdependent subsystems (Fig. 2). The fuselage of an RC helicopter, being small and lightweight, can be treated as a single rigid body to which general rules of rigid body dynamics apply. Equation (2) shown at the bottom of this page, shows the interdependence of fuselage states and the role of net external forces $\{X, Y, Z\}$ and moments $\{L, M, N\}$ acting along the helicopter's orthogonal axes (Fig. 1). Here, M_H , $I_{\{xx,yy,zz,xz\}}$, and g represent the mass, the components of the inertia matrix of the helicopter, and acceleration due to gravity, respectively. This paper models instantaneous local wind flow \mathbf{w}_r at any general point location \mathbf{r} relative to the main rotor hub in the helicopter's frame of

reference using a six-parameter linear model as [23], [27]

$$\mathbf{w}_r = \boldsymbol{\omega} \times \mathbf{r} + \mathbf{v} \quad \left| \quad \boldsymbol{\omega} = [\omega_x \ \omega_y \ \omega_z]^T, \mathbf{v} = [v_x \ v_y \ v_z]^T. \quad (3)$$

Here \times represent a vector cross product, and $\boldsymbol{\omega}$ and \mathbf{v} represent sets (vectors) of the wind vorticities and mean flow along the three axes of the helicopter's frame of reference. Helicopters generate control forces and moments through a collective interaction of wind with its various body parts. The net helicopter forces and moments can be categorized on the basis of the part involved in the interaction with the wind:

$$\mathbf{F} = \mathbf{F}_{mr} + \mathbf{F}_T + \mathbf{F}_f + \mathbf{F}_e = [X \ Y \ Z]^T$$

$$\mathbf{M} = \mathbf{M}_{mr} + \mathbf{M}_T + \mathbf{M}_f + \mathbf{M}_e = [L \ M \ N]^T. \quad (4)$$

Here \mathbf{F} and \mathbf{M} represent force and moment vectors and the subscripts mr, tr, f, and e represent “main rotor,” “tail rotor,” “fuselage,” and “empennage,” respectively. Fig. 2 shows different constituent subsystems of the proposed helicopter dynamics model. Each of these helicopter dynamics components, which depend on both local wind conditions and pilot inputs, has been individually discussed in the subsequent subsections of this paper.

B. Main Rotor Dynamics

Out of all the control components, the effect of external wind conditions is most prominent in the main rotor dynamics. The wind relative to the main rotor consists of components arising from both helicopter motions (including rotor inflow) and external wind flow (air wake). The internally generated perpendicular (\bar{U}_{PH}) and tangential (\bar{U}_{TH}) components of the wind relative to the rotor blades at a normalized radial distance \bar{r}_b on the rotor position ψ_b can be computed as:

$$\begin{bmatrix} \bar{U}_{PH} \\ \bar{U}_{TH} \end{bmatrix} = \begin{bmatrix} -\lambda_0 - R\bar{r}_b\beta' + R\bar{r}_bp \sin \psi_b + (R\bar{r}_bq - \lambda_c) \cos \psi_b \\ R\bar{r}_b\Omega + R\bar{r}_b\zeta' \end{bmatrix} \times \frac{1}{R\Omega} \quad (5)$$

where β' and ζ' are the partial derivatives of the rotor flapping angle β and lead-lag angle ζ , respectively, relative to the rotor azimuth position ψ_b and $\{\lambda_0, \lambda_c\}$, which represent parameters of the linear static inflow model. The effect of the yaw rate (r) of the helicopter has been ignored in the \bar{U}_{TH} term since $r \ll \Omega$.

Similarly, using the linear model (3) the perpendicular (\bar{U}_{PW}) and tangential (\bar{U}_{TW}) components of the external wind flow

$$f(\mathbf{x}, \dot{\mathbf{x}}, \mathbf{w}, \mathbf{u}) = \mathbf{0} \quad \left\{ \mathbf{x} \in \mathbf{R}^{30}, \mathbf{w} \in \mathbf{R}^6, \mathbf{u} \in \mathbf{R}^4 \right\}; \quad \mathbf{x} = [\mathbf{B} \ \mathbf{F} \ \mathbf{L} \ \mathbf{I} \ \mathbf{P}]^T, \quad \mathbf{u} = [\delta_0 \ \delta_c \ \delta_s \ \delta_T]^T, \quad \mathbf{w} = [\mathbf{v}_x \ \mathbf{v}_y \ \mathbf{v}_z \ \omega_x \ \omega_y \ \omega_z]^T$$

$$\mathbf{B} = [u \ v \ w \ \theta \ \varphi \ \psi \ p \ q \ r]^T, \quad \mathbf{F} = [\beta_0 \ \dot{\beta}_0 \ \beta_c \ \dot{\beta}_c \ \beta_s \ \dot{\beta}_s]^T, \quad \mathbf{L} = [\zeta_0 \ \dot{\zeta}_0 \ \zeta_c \ \dot{\zeta}_c \ \zeta_s \ \dot{\zeta}_s]^T, \quad \mathbf{I} = [\lambda_0 \ \lambda_c \ \chi]^T, \quad \mathbf{P} = [\theta_0 \ \theta_c \ \dot{\theta}_c \ \theta_s \ \dot{\theta}_s \ \theta_T]^T \quad (1)$$

$$\begin{aligned} \dot{u} &= X/M_H - (wq - vr) - g \sin \theta & I_{xx}\dot{p} &= qr(I_{yy} - I_{zz}) + I_{xz}(\dot{r} + pq) + L & \dot{\varphi} &= p + (q \sin \varphi + r \cos \varphi) \tan \theta \\ \dot{v} &= Y/M_H - (ur - wp) + g \cos \theta \sin \varphi & I_{yy}\dot{q} &= rp(I_{zz} - I_{xx}) + I_{xz}(r^2 - p^2) + M & \dot{\theta} &= q \cos \varphi - r \sin \varphi \\ \dot{w} &= Z/M_H - (vp - uq) - g \cos \theta \cos \varphi & I_{zz}\dot{r} &= pq(I_{xx} - I_{yy}) + I_{xz}(\dot{p} - qr) + N & \dot{\psi} &= (q \sin \varphi + r \cos \varphi) \sec \theta \end{aligned} \quad (2)$$

relative to the rotor hub at a radial distance \bar{r}_b and azimuth position ψ_b can be estimated as

$$\begin{bmatrix} \bar{U}_{PW} \\ \bar{U}_{TW} \end{bmatrix} = \begin{bmatrix} -v_z - R\bar{r}_b\omega_y \cos \psi_b - R\bar{r}_b\omega_x \sin \psi_b \\ -v_y \cos \psi_b + v_x \sin \psi_b - R\bar{r}_b\omega_z \end{bmatrix} \frac{1}{R\Omega}. \quad (6)$$

The net forces and moments exerted by the main rotor on the helicopter fuselage can be obtained by the integration of the aerodynamic lift and drag forces along the blade length. Equation (7) shown at the bottom of this page, shows the normalized differential lift (F_L) and drag (F_D) forces as a function of relative wind and main rotor pitch angle (θ_b). Here, δ , C_T , and a_0 represent the aerodynamic drag coefficient, rotor thrust coefficient, and lift curve slope for the main rotor blade, respectively. The aerodynamic coefficients were obtained using the NACA0012 airfoil model [28]. The aerodynamic interactions of the moving rotor blades with respect to the local wind result in periodic in-plane (lead-lag) and out-of-plane (flapping) motion of the rotor blades relative to the rotating hub.

1) Rotor Flapping and Lead-Lag: The vertical component of the spatially varying lift and drag forces acting on the rotor blades results in “out-of-the-plane” flapping while rotating about the rotor hub. For simplified computations, the flapping has been modeled using the center-spring equivalent model [6], [7], [25] with the solution assumed to be limited to the first-order harmonics in the multiblade coordinate system. The flapping parameters $\{\beta_0, \beta_c, \beta_s\}$ can be estimated by solving the blade flapping dynamics (8), with aerodynamic damping and nonuniform static rotor inflow conditions after higher order harmonics are ignored.

$$\begin{aligned} \beta'' + \lambda_\beta^2 \beta &= 2(\bar{p} \cos \psi_b - \bar{q} \sin \psi_b) + \frac{\gamma}{2} \int_{\bar{r}_b=0}^1 (F_L \bar{r}_b) d\bar{r}_b; \\ \lambda_\beta^2 &= 1 + K_\beta / (I_\beta \Omega^2); \gamma = \rho c a_0 R^4 / I_\beta; \\ \bar{p} &= p / \Omega; \bar{q} = q / \Omega \end{aligned} \quad (8)$$

Here, γ is the lock number of the helicopter (ratio of aerodynamic to inertia forces acting on a rotor blade), ρ is the air density, I_β and K_β are the moment of inertia and equivalent spring stiffness constant of the rotor blades (determined experimentally), and λ_β is the flapping frequency ratio. The flapping parameters obtained from (7) are a function of both helicopter states and the local wind parameters w .

Similar to flapping, the rotor lag can also be modeled using the center-spring equivalent model. The lead-lag parameters $\{\zeta_0, \zeta_c, \zeta_s\}$ can be estimated by solving the in-plane dynamics of the main rotor blades (9).

$$\zeta'' + \lambda_\zeta^2 \zeta = -\frac{1}{2} \gamma \int_{\bar{r}_b=0}^1 (F_D \bar{r}_b) d\bar{r}_b; \quad \lambda_\zeta^2 = \frac{3}{2} \left(\frac{e_\zeta}{1 - e_\zeta} \right). \quad (9)$$

Here λ_ζ is the lead-lag frequency ratio and e_ζ is the normalized lag hinge offset. Aerodynamic damping arises from the presence of ζ' term in (5). Due to relatively low values of the flapping angles and their time derivatives, the Coriolis coupling between the flapping and lead-lag motion has been ignored here.

2) Main Rotor Forces and Moments: The differential forces acting on the rotor blades can be integrated to estimate the net main rotor forces (\mathbf{F}_{mr}) acting on the helicopter's rotor hub as

$$\begin{aligned} \mathbf{F}_{mr} &= \frac{\gamma I_\beta \Omega^2}{2R} \sum_{i=1}^{N_b} \begin{bmatrix} F_D s \psi_{bi} + \beta_i F_L c \psi_{bi} \\ F_D c \psi_{bi} - \beta_i F_L s \psi_{bi} \\ F_L \end{bmatrix}; \\ \begin{cases} F_L = - \int_{\bar{r}_b=0}^1 U_L d\bar{r}_b \\ F_D = - \int_{\bar{r}_b=0}^1 U_D d\bar{r}_b \end{cases} \end{aligned} \quad (10)$$

Here s and c represent trigonometric sine and cosine functions, subscript i represents quantities corresponding to the i_{th} main rotor blade, and N_b represents the number of the blades in the rotor. Similar to the process of the flap and lag estimation, the integrals F_L and F_D are simplified by ignoring the third-order and higher order harmonics. The main rotor moments (\mathbf{M}_{mr}) can be obtained from center-spring equivalent flapping and lag estimates and main rotor forces as shown below [25].

$$\mathbf{M}_{mr} = -\frac{N_b}{2} [K_\beta \beta_s \quad K_\beta \beta_c \quad K_\zeta \zeta]^T + [0 \ 0 \ -h_R]^T \times \mathbf{F}_{mr} \quad (11)$$

Here h_R is the location of the rotor hub in the helicopter's frame of reference and \times represents 3-D vector cross product. Both \mathbf{F}_{mr} and \mathbf{M}_{mr} together form the most critical component of the helicopter dynamics estimates (4).

C. Tail Rotor Dynamics

The tail rotor blades of an RC helicopter, being smaller than the main rotor blades, do not produce sufficient thrust to generate significant modes in the blades or induce inflow. In such conditions, the external wind flow can be assumed uniform over the tail rotor disk area. Equation (12) shown at the bottom of the next page, shows the expression of the force \mathbf{F}_T and moment \mathbf{M}_T produced by the tail rotor (located at position vector \mathbf{r}_T) in the helicopter's frame of reference. Here, subscript T indicates quantities related to the tail rotor and the variables ρ , R_T , Ω_T , c_T , and a_{0T} represent the air density, rotor length, rotor speed, rotor blade chord length, and lift curve slope, respectively.

D. Fuselage/Empennage Dynamics

The fuselage of the helicopter primarily contributes to the helicopter dynamics in the form of aerodynamic drag forces.

$$\begin{aligned} F_L &= \bar{U}_T^2 \theta_b + \bar{U}_T \bar{U}_P \quad \text{and} \quad F_D = \bar{U}_P^2 + \bar{U}_T \bar{U}_P \theta_b - \delta \bar{U}_T^2 / a_0 \\ \text{where, } \bar{U}_T &= \bar{U}_{TH} + \bar{U}_{TW}, \bar{U}_P = \bar{U}_{PH} + \bar{U}_{PW}, \delta = \delta_0 + \delta_2 C_T^2 \end{aligned} \Rightarrow \begin{cases} F_L \approx (\bar{U}_{TH}^2 + 2\bar{U}_{TH}\bar{U}_{TW})\theta_b + \bar{U}_{TH}\bar{U}_{PH} \\ \quad + \bar{U}_{TH}\bar{U}_{PW} + \bar{U}_{PH}\bar{U}_{TW} \\ F_D \approx (\bar{U}_{TH}\bar{U}_{PH} + \bar{U}_{TH}\bar{U}_{PW} + \bar{U}_{PH}\bar{U}_{TW})\theta_b \\ \quad - \delta(\bar{U}_{TH}^2 + 2\bar{U}_{TH}\bar{U}_{TW})/a_0 \end{cases} \quad (7)$$

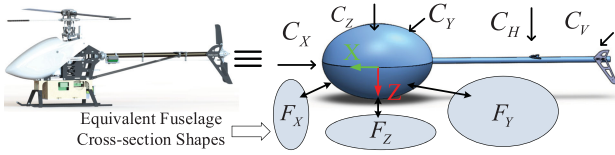


Fig. 3. Helicopter's equivalent shape and aerodynamic drag surfaces.

The drag forces can be computed by modeling the shape of the helicopter fuselage as a tri-axial ellipsoid (with axial lengths 48 cm \times 37 cm \times 19 cm). In a study conducted by J. A. DeMoss [29], aerodynamics drag coefficients of an ellipsoidal body were experimentally measured. As the helicopter's shape closely resembles an ellipsoid, the drag coefficients of the ellipsoid can be used for the helicopter's fuselage computation. Fig. 3 shows the equivalent shape and drag surfaces of the helicopter fuselage. Here, the three adjacent ellipses represent the face cross-sections (F_X , F_Y , and F_Z) of the fuselage. The drag force (F_f) experienced by the fuselage can be estimated as follows, where the terms C_X , C_Y , and C_Z represent equivalent drag coefficients for winds flowing in the three axes of the helicopter.

$$\mathbf{F}_f = \frac{\rho}{6} \begin{bmatrix} C_X(u + v_x)^2 \\ C_Y(v + v_y)^2 \\ C_Z(w + v_z - v_d)^2 \end{bmatrix}; \quad (13)$$

$$\begin{cases} C_X = C_{DL}L_x^2 + C_{DF}F_x + C_{DW}W_x \\ C_Y = C_{DL}L_y^2 + C_{DF}F_y + C_{DW}W_y \\ C_Z = C_{DL}L_z^2 + C_{DF}F_z + C_{DW}W_z \\ v_d = \lambda_0 + \sqrt{T/(2\rho A_d)} \end{cases}$$

Here, the terms C_{DL} , C_{DF} , and C_{DW} represent drag coefficients for and corresponding to the ellipsoid length (L), face cross-section area (F), and wetting area (W) relative to the incident wind gust. As the shape of the helicopter is symmetric about the center, the moments arising from the unbalanced fuselage drag (M_f) can be ignored.

In addition to the fuselage, the empennage (vertical and horizontal stabilizer fins) also causes significant drag forces on the helicopter (Fig. 3). The RC helicopter used in the presented study, has one horizontal fin on the tail boom and one vertical fin besides the tail rotor. The net force and moments acting on the helicopter due to the drag forces on the stabilizer fins are computed as

$$\mathbf{F}_e = \frac{\rho}{2} \begin{bmatrix} 0 \\ C_{VF}(v + v_y - rl_T + \sqrt{F_T/(2\rho A_{dt})})^2 \\ C_{HF}(\lambda_0 + \sqrt{T/(2\rho A_d)} + w + v_z + ql_H)^2 \end{bmatrix}$$

$$\mathbf{M}_e = [0 \quad F_{e3}l_H \quad -F_{e2}l_T]^T \quad (14)$$

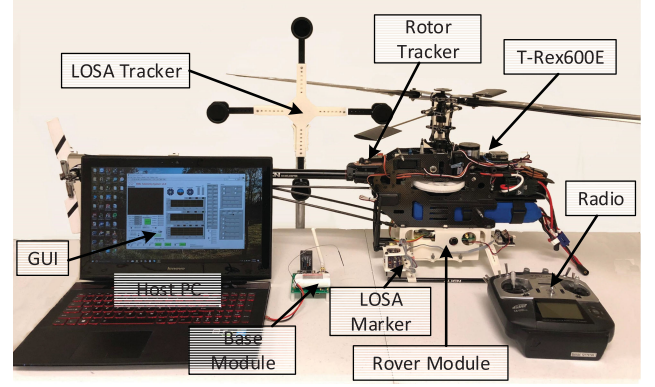


Fig. 4. Hardware setup for the proposed system.

Here, C_{HF} and C_{VW} represent the vane drag coefficients for the horizontal and the vertical fins, respectively (obtained using CFD studies done in Comsol software package), and A_{dT} represents the tail rotor disk area of the helicopter.

E. Stabilizer/Flybar Dynamics

RC helicopters are often equipped with a flybar assembly to improve the stability of the UAV. Flybar dynamics are necessary for modeling the helicopter's dynamics, as the actual cyclic main rotor pitch angles depend on the seesaw flapping angle of the flybar. Adapting the stabilizing bar model presented in [26], the main rotor blade pitch angles can be estimated as shown in (15) at the bottom of the next page. The terms Ω , μ , μ_z , and λ represent rotor speed, forward advance ratio, axial advance ratio, and main rotor inflow, respectively. The independent variables γ_f , η_2 , c_1 , and c_2 represent flybar blade lock number, thrust scaling factor, and fractional contribution of the swashplate and flybar tilting in the main rotor blade pitch angles, respectively. The rotor blade pitch angles obtained by solving (15) can be fed into the helicopter forces/moment model (4) to estimate the pilot-induced dynamics.

The above described the force/moment components (which depend on both pilot inputs and ambient wind conditions) that collectively govern the helicopter's fuselage dynamics (2) and can be compared against the helicopter's inertial measurement unit (IMU) measurements to estimate wind conditions.

III. TELEMETRY SYSTEM AND EXPERIMENTAL SETUP

The telemetry system hardware comprises two independent instrumentation subsystems called the rover module (retrofitted on an Align T-Rex 600E RC helicopter) and the base module [23]. Fig. 4 shows the hardware setup of the proposed telemetry

$$\begin{aligned} \mathbf{F}_T &= [0 \quad -Y_T \quad 0]^T \Rightarrow \left\{ Y_T = \frac{\rho c_T a_{0T} R_T^3 \Omega_T^2 N_b}{2} \left(\frac{\theta_{3T}}{3} + \frac{(v_{T1}^2 + v_{T3}^2) \theta_T}{2\Omega_T^2 R_T^2} + \frac{v_{T2}}{2\Omega_T R_T} \right) \right. \\ \mathbf{M}_T &= \mathbf{r}_T \times \mathbf{F}_T \quad \left. \mathbf{r}_T = [-l_T \quad 0 \quad -h_T]^T, \Omega_T = N_T \Omega \right\} \end{aligned} \quad (12)$$

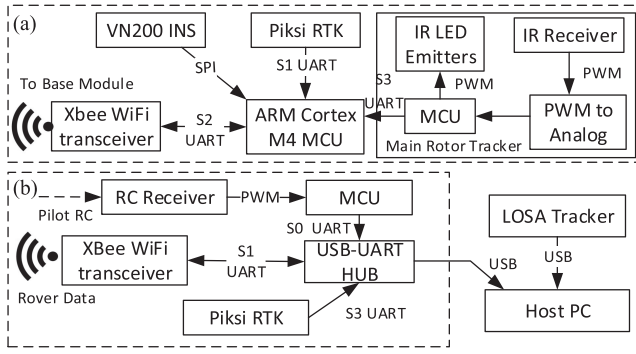


Fig. 5. Electrical Schematics of (a) rover module, (b) base module.

system. The proposed telemetry system is supplemented by a custom-made linear optical sensor arrays (LOSA) motion tracking system [30], [31] for obtaining (millimeter level) accurate position and attitude estimates relative to the wind source at an update rate of >300 Hz.

Fig. 5 shows the electrical schematic diagram of both the rover and base modules. The base module is equipped with an RC receiver (similar to the one used for controlling the helicopter) to record the pilot inputs. The rover module uses VN200 INS as the primary inertial sensor and includes a rotor tracking subsystem to measure the main rotor speed during flight. The main rotor tracker (attached to the helicopter fuselage) beams high-frequency IR light pulses upwards (at moving rotor blades) and detects IR reflections from the rotor blades using TSMP6000 IR sensor module. The subsystem then measures the time interval between the two consecutive reflections to estimate the rotor speed. The rover module also measures the pulsewidth modulation commands from the heading stabilization system to the helicopter's tail actuator and relays them to the base module along with the rest of the telemetry data.

The experimental setup (shown in Fig. 6) primarily comprises two large opposing (24-inch diameter) wind circulation fans (with adjustable speeds), separated at a fixed distance and at different heights and a T-Rex600E RC helicopter with a rover module and LOSA tracker retrofitted on it. The host PC receives and records the time-stamped helicopter dynamics, position estimates, and pilot input data from the rover module, the base module, and the LOSA tracking system, respectively, for post processing.

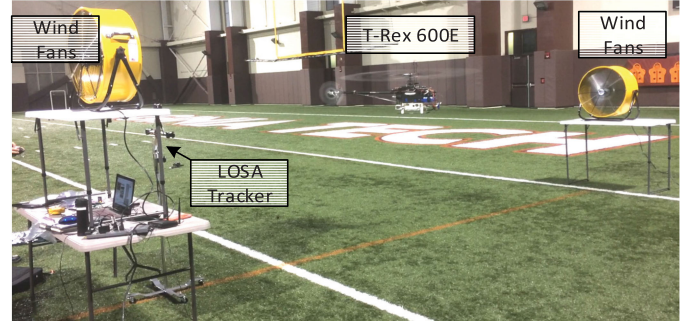


Fig. 6. Experimental setup for the presented study.

IV. MODEL PARAMETERS OPTIMIZATION

As described in (1), (2), and (4), the RC helicopter dynamics model depends on nearly 37 different parameters in addition to the wind conditions and pilot inputs. These model parameters (as shown in Table I) were obtained from different sources with different accuracy/confidence levels. In order to obtain an accurate dynamics model, the system model parameters were optimized using flight data collected in a large indoor facility (Fig. 6) in still air conditions (wind circulation fans switched off). To collect the calibration data, the helicopter was flown at an altitude of more than two rotor diameters (~ 2.5 m), to eliminate any rotor-ground effect. Furthermore, a variety of high dynamics maneuvers and oscillatory tilting motions (at varying frequency) were performed to create a versatile dataset of pilot input combinations, along with other state variables and dynamics measurements. The helicopter model presented in the previous section can be used to estimate translational and rotational acceleration of the given RC helicopter. These acceleration estimates can be compared against IMU acceleration measurements for the assessment of the model parameters. This study explores Particle Swarm Optimization (PSO) algorithm for optimizing the helicopter model parameters.

A. Particle Swarm Optimization

PSO is essentially a nongradient stochastic sampling based on multidimensional global optimization algorithm, mimicking the swarm intelligence of bird flocks [32]. Each particle involved in the PSO is defined by a vector in the multidimensional search space with random initialization and can be used to individually compute helicopter dynamics in the form of translational and angular acceleration (including gravity, as measured by the

$$\begin{aligned} \begin{bmatrix} \ddot{\theta}_c \\ \ddot{\theta}_s \end{bmatrix} + \mathbf{A}_\theta \Omega \begin{bmatrix} \dot{\theta}_c \\ \dot{\theta}_s \end{bmatrix} + \mathbf{A}_\theta \Omega^2 \begin{bmatrix} \theta_c \\ \theta_s \end{bmatrix} &= \mathbf{B}_{\omega_H} \Omega^2 \begin{bmatrix} \bar{p} \\ \bar{q} \end{bmatrix} + \mathbf{B}_\delta \Omega^2 \begin{bmatrix} \delta_c \\ \delta_s \end{bmatrix} + \mathbf{B}_\lambda \Omega^2 [(\mu_z - \lambda_0) \lambda_c \lambda_s]^T \\ \text{where, } \left\{ \mathbf{B}_\lambda = \frac{\gamma_f}{8c_2} \begin{bmatrix} 2\eta_2\mu & 0 & -1 \\ 0 & 1 & 0 \end{bmatrix}, \mathbf{A}_\theta = \frac{1}{8} \begin{bmatrix} \gamma_f & 16 \\ -16 & \gamma_f \end{bmatrix}, \mathbf{A}_\theta = \frac{\gamma_f}{8} \begin{bmatrix} 0 & 1 - \frac{1}{2}\eta_2\mu^2 \\ -1 - \frac{1}{2}\eta_2\mu^2 & 0 \end{bmatrix}, \right. \\ \left. \mathbf{B}_{\omega_H} = \frac{1}{c_2} \begin{bmatrix} \gamma_f & -16 \\ -16 & \gamma_f \end{bmatrix}, \text{ and } \mathbf{B}_\delta = \frac{\gamma_f}{8c_2} \begin{bmatrix} 0((1+c_1) + \frac{1}{2}(3+c_1)\eta_2\mu^2) \\ -((1+c_1) + \frac{1}{2}(1-c_1)\eta_2\mu^2) & 0 \end{bmatrix} \right\}. \end{aligned} \quad (15)$$

TABLE I
HELICOPTER MODEL INITIAL AND FINAL VARIABLES/PARAMETERS

Var.	Initial Value	Uncertainty	Final Value	Units	Var.	Initial Value	Uncertainty	Final Value	Units	Var.	Initial Value	Uncertainty	Final Value	Units
R^*	6.730	30%	6.664	10^{-1} m	I_{xx}^{\ddagger}	3.173	50%	3.834	10^{-1} kg.m ²	C_X^{\ddagger}	6.26	50%	5.760	10^{-2} Nms ² /kg
R_T^*	1.3	30%	1.303	10^{-1} m	I_{zz}^{\ddagger}	1.539	50%	1.440	kg.m ²	C_Y^{\ddagger}	1.036	50%	1.002	10^{-1} Nms ² /kg
c_T^*	2.7	0%	2.7	10^{-2} m	c^*	5.4	0%	5.4	10^{-2} m	C_Z^{\ddagger}	2.43	50%	2.573	10^{-2} Nms ² /kg
γ	4.486	100%	3.393	-	I_{xz}^{\ddagger}	-5.19	50%	-5.21	10^{-2} kg.m ²	C_{HF}^{\ddagger}	7.598	50%	8.140	10^{-4} Ns ² /m ²
δ_0^{\ddagger}	7.303	40%	7.02	10^{-2}	Ω^*	1.633	0%	1.672	10^2 rad/s	C_{VF}^{\ddagger}	2.2	50%	2.105	10^{-3} Ns ² /m ²
h_T^{\ddagger}	1.2	30%	1.197	10^{-2} m	h_R	2.1	30%	2.049	10^{-1} m	K_c	1.488	200%	2.870	10^2 Nm/rad
ρ^*	1.225	0%	1.225	kg/m ³	e_c	1.071	30%	1.042	10^{-1}	K_β	8.42	350%	29.71	10^1 Nm/rad
N_T^*	3.85	0%	3.85	-	A_{dT}	3.3	30%	3.310	10^{-2} m ²	a_0^{\ddagger}	6.082	100%	2.874	NmJ ⁻¹ rad ⁻¹
γ_f	8.002	50%	8.010	10^{-1}	g^*	9.798	0%	9.798	m/s ²	a_{0T}^{\ddagger}	6.08	100%	7.091	NmJ ⁻¹ rad ⁻¹
l_T^{\ddagger}	7.9	30%	7.978	10^{-1} m	A_d	1.4116	30%	1.4134	m ²	δ_2^{\ddagger}	4.912	50%	4.646	10^{-3}
c_1^*	7.33	0%	7.33	10^{-1}	M_H^*	4.975	0%	4.975	kg	l_H^{\ddagger}	5.7	30%	5.567	10^{-1} m
c_2^*	6.63	0%	6.63	10^{-1}	I_{yy}^{\ddagger}	1.483	50%	1.315	kg.m ²	I_β	1.84	50%	1.931	10^{-2} kg.m ²
η_2^*	4.371	0%	4.371	-										

*Direct measurement/constant. †From cited studies. ‡From CAD/CFD models.

accelerometer) in the helicopter's local frame of reference. During the optimization process, all particles keep track of their individual best performance and the global best performance (among all particles). All particles update their current value by comparing against their individual and global best particles. To update any i th particle (X^i) in the swarm, the velocity (V^i) estimates in the k th iteration can be estimated from the individual particle's best performance (X_{ib}) and the global best particle (X_{gb}), respectively, as

$$\begin{aligned} X_k^i &= X_{k-1}^i + V_k^i \\ V_N^i &= mV_{k-1}^i + C_1r_1(X_{ib}^i - X_{k-1}^i) + C_2r_2(X_{gb} - X_{k-1}^i). \end{aligned} \quad (16)$$

Here, m (0.1) is the inertia coefficient, C_1 , C_2 (each 0.2) are exploitation coefficients, and r_1 , r_2 are exploration coefficients (random numbers generated between 0 and 1). To optimize the model parameters, a swarm of 2000 randomly initialized particles was deployed with each particle dimension limited to the bounds determined by an uncertainty in their initial values, which depends on the data source reliability. These uncertainty bounds were determined through empirical observations during multiple trials with PSO training. Uncertainty bound for any variable was increased appropriately whenever the PSO failed to converge while hitting that variable's bounding limit. Table I shows the final values of the variable along with uncertainties in their initial values. K_β showed maximum deviation from its expected initial value, which comes from the fact that the rotor blades on the helicopter are not fully articulated but hinged. Fig. 7 shows the flow diagram of the PSO algorithm while focusing on a single particle. The green ellipses represent particles (37-dimensional vector) and the orange ellipses represent the norm of error in acceleration estimation (scalar value). As some parameters of the helicopter model were known with absolute certainty (constants/experimentally measured), particle velocity corresponding to such parameters were ignored and set to zero. Despite having constant values, these parameters were modeled as variables (with zero uncertainty) for ease in software architecture development and compatibility with different types

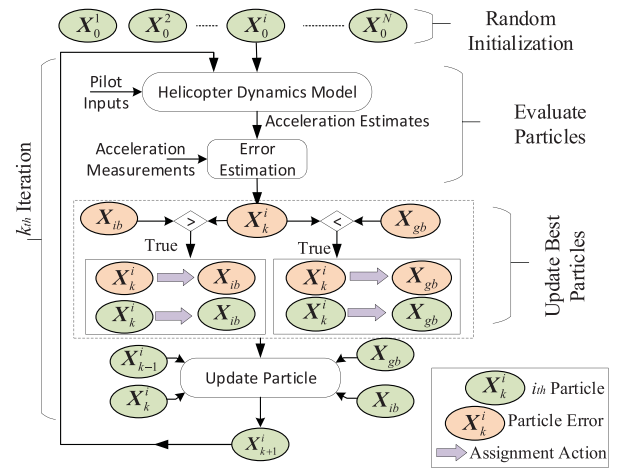


Fig. 7. Operations flowchart of the PSO algorithm.

of helicopters. The global best particle represents the output of the PSO algorithm at any point in time.

B. Optimization Results

Fig. 8 shows the PSO performance results on a calibration flight of ~ 62 000 samples (in external wind free environment) over 500 iterations. Fig. 8(a) shows an asymptotic decrease in the norm of the modeling error of the helicopter acceleration (translational and rotational combined) with process iterations with an rms estimation error value of 0.848 (units ignored). Fig. 8(b) shows the error distribution in the form of an error histogram (log scale) for the prediction of all the six acceleration channels. Fig. 8(c) shows acceleration estimates obtained from the optimized models plotted against the IMU measurements along with pilot inputs. A very good fit was observed between the estimated and measured accelerations (both translational and rotational) with the PSO-optimized model. PSO is often expected to outperform gradient descent (GD) based optimization methods that are prone to premature convergence at local minima. GD-based methods are also very sensitive to the initial parameter vector (position), unlike PSO, which simultaneously

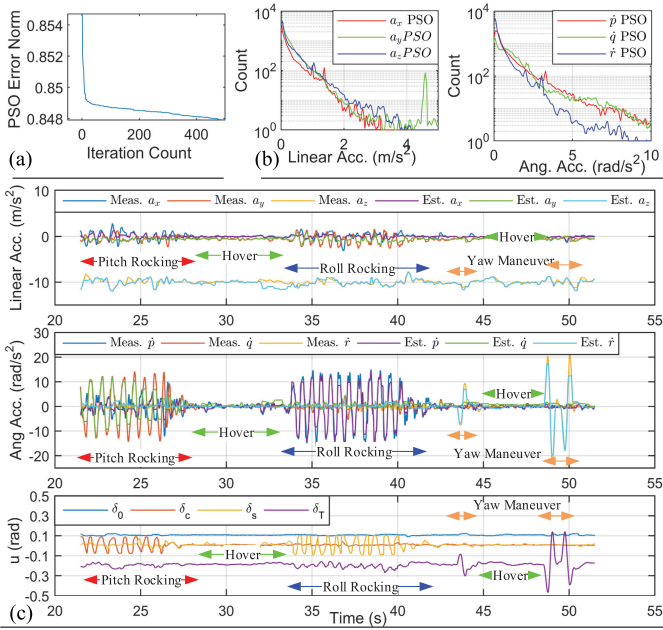


Fig. 8. Particle swarm optimization results. (a) Modeling error progression. (b) Model error distribution. (c) Model output along with pilot inputs (u).

search at multiple positions. Thus, to obtain reliable wind estimates, a globally optimized dynamics model parameters obtained from the PSO have been used for the subsequent studies.

V. WIND ESTIMATION AND RESULTS

To test the capability of the proposed system in wind estimation, the helicopter was flown in a controlled environment with known wind conditions (Fig. 6). Turbulent wind flow field was generated by the two opposing wind circulation fans. The wind flow pattern was measured using the setup presented in [23], [27] using a three-axis Young Ultrasonic Anemometer (Model 81000) [33] mounted on a pole with an adjustable height (Fig. 9(a)). The LOSA motion tracking system [30] was used to localize wind measurements and map the wind field in the global (wind source) frame of reference. Attitude and velocity estimates from the motion tracker were further used to compensate for the motion of the anemometer in the wind measurements. As discussed in [23], the wind measurements were taken at (~ 130) different locations and for at least 10 s of duration. Fig. 9(b) and (c) shows the direction and magnitude mean (steady-state) wind flow field using matrices of 3-D arrows (interpolated at a grid of size 5 cm) obtained by using the setup shown in Fig. 9(a). Fig. 9(b) shows the 3-D spatial distributions of the steady-state wind speed. As shown in the figure, the steady-state wind speed reaches up to 4 m/s. Similarly, Fig. 9(c) shows the spatial distribution of the turbulence (with root mean square value reaching up to 2.1 m/s) in the artificiality generated flow field. To characterize the wind flow for further analysis, the six-parameter linear model w ((3)) was fitted to the local steady-state wind flow field in a volume of $1.3 \text{ m} \times 1.3 \text{ m} \times$

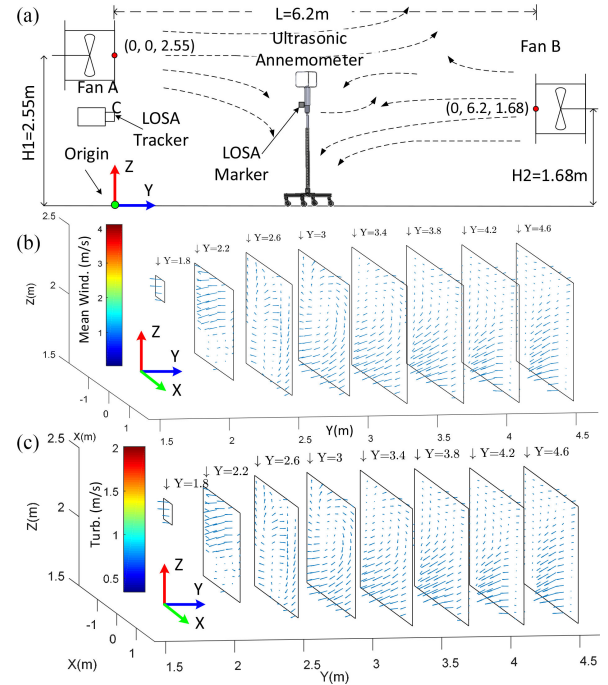


Fig. 9. Wind mapping experiment. (a) Experiment setup. (b) Steady-state wind map. (c) Wind turbulence map.

0.6 m (equivalent to the helicopter's size) using the least squares method. As the wind parameters were computed on the basis of the steady-state component of the wind flow, the turbulence in the flow acts as a modeling noise in the wind parameters. This paper proposes to use APFs for the estimation of instantaneous wind flow field characterized by w .

A. Active Particle Filters

APFs are model-based tracking algorithms that use sequential Monte Carlo simulation for representation of probability densities [34]–[36]. APF is a type of recursive filter that uses simulated samples in the search state space (particles) with associated weights to represent the probability distribution of the random variable. The system is solved for each particle to obtain its fitness value (weighting coefficient). Let χ be a set of N weighted samples, then for each iteration the probability distribution function (pdf) of random variable x can be estimated as.

$$\bar{x} = E(\chi) = \sum_j x_j p(x_j) \text{ where } \chi = \{x_j, w_j\}_{j=1..N}$$

$$w_j = \exp\left(-\frac{1}{\sigma} \|\mathbf{z} - \hat{\mathbf{z}}\|\right) \text{ and } p(x) = \sum_j w_j \cdot \delta_{x_j}(x). \quad (17)$$

where δ is the Delta-Dirac function for sample x_j

Here w_j represents the fitness value (weighting coefficient) of the j th particle computed from the measured states (\mathbf{z}) and expected values of the measured states ($\hat{\mathbf{z}}$, using the system model) with σ being an error sensitivity factor. The expected value to the random state variable (\bar{x}) is estimated from the expected value of particles of the value of the pdf $p(x)$. After each

iteration, the particles are updated using $p(x)$ through Monte-Carlo regularization method.

B. Wind Estimation Using APF

APFs are an ideal estimation tool for nonlinear systems without requiring prior knowledge of the states to be estimated. Since the turbulent wind flow is a highly stochastic quantity to model statistically, the proposed system uses APFs for the estimation of wind characterization parameters (w). To estimate the wind conditions, an APF with a population of 2000 (six-dimensional) particles was randomly initialized to thoroughly scan the search space. Each dimension of the particle was normalized to a value between 0 and 1 based on the extreme values of the wind parameters measured experimentally. For each particle, the linear $\{a_x, a_y, a_z\}$ and rotational $\{\dot{p}, \dot{q}, \dot{r}\}$ accelerations were estimated using the pilot inputs and state measurements and wind condition (from the concerned particles) with the helicopter's model presented in Section II. The estimated accelerations (\hat{z}) are compared against the acceleration measured using the IMU (z) to identify the "well-performing" particle and estimate the wind condition parameters from the expected value of $p(x)$ over populations (17). For the subsequent iterations, the "fittest" particles are the randomly selected particles using the roulette wheel method. This process continues recursively for all input samples.

C. Results and Discussions

The 6-D wind parameters obtained using the APFs are essentially the result of the dynamics assessment of the helicopter and hence are represented in the helicopter's local frame of reference. To obtain external wind flow parameters, the wind parameters were converted from the local frame to the inertial frame of reference using the attitude estimates obtained from the LOSA tracker. Fig. 10 shows the mean wind flow field in the form of 3-D slice plots of the velocity components $\{v_x, v_y, v_z\}$ obtained from the proposed system and the wind map generated using anemometer measurements. For each subplot, the velocity data are plotted on six planes (namely A-F, representing $Y = \{2.2, 2.6, 3.0, 3.4, 3.8, 4.2\}$) in XZ planes. Similar to the mean velocity field, Fig. 11 shows the wind vorticity $\{\omega_x, \omega_y, \omega_z\}$ distribution obtained from the proposed system and anemometer generated map. A good correlation is visible in the $v_x, v_y, \omega_x, \omega_y,$ and ω_z distributions obtained from the proposed system and anemometer maps.

For more quantitative analysis, the estimated mean velocity and vorticity distributions were compared against steady-state anemometer readings. There are three main reasons behind this behavior. First, in the present study, it was assumed that the rotor wakes are negligible in the inflow modeling (visible in v_z distribution). Second, unlike the anemometer, the helicopter was not stationary during experiments. Therefore, the interpolation process captured the turbulence transients in the dynamics, making the estimates discontinuous. Third, the reference wind parameters were obtained from the steady-state component of the wind flow field (measured using anemometer) and ignored the temporally varying turbulence factor. Fig. 12

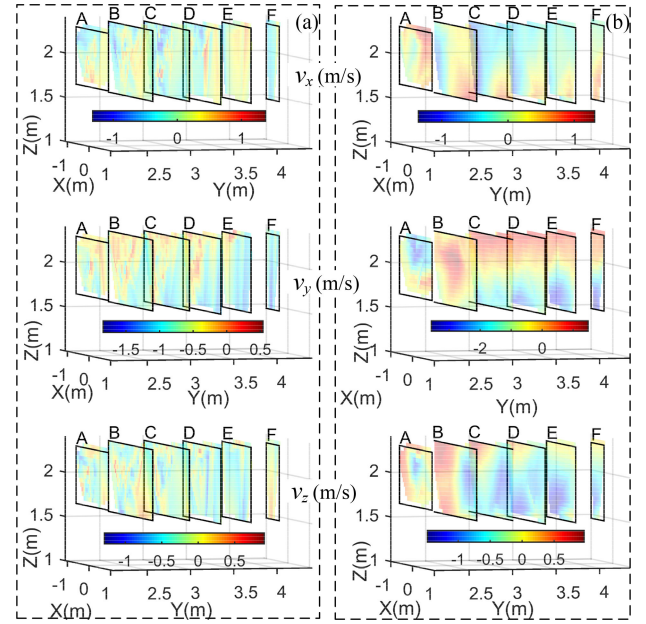


Fig. 10. Mean wind flow map using (a) proposed system, (b) anemometer.

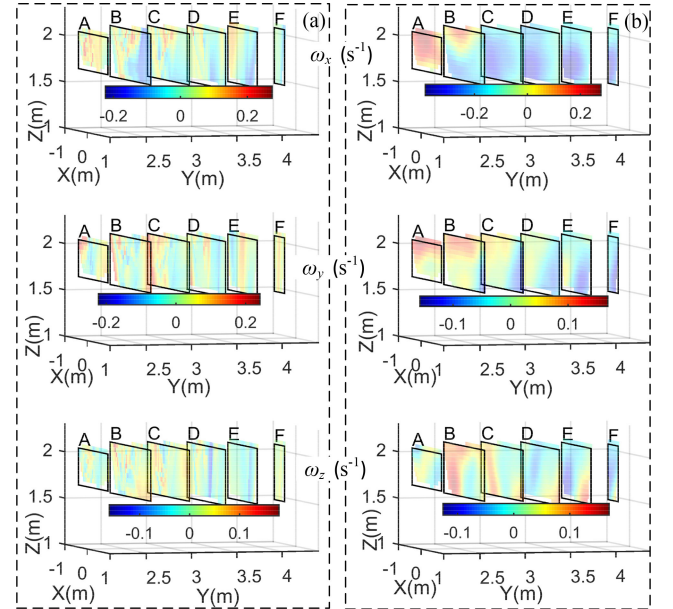


Fig. 11. Vorticity map using (a) proposed system, (b) anemometer.

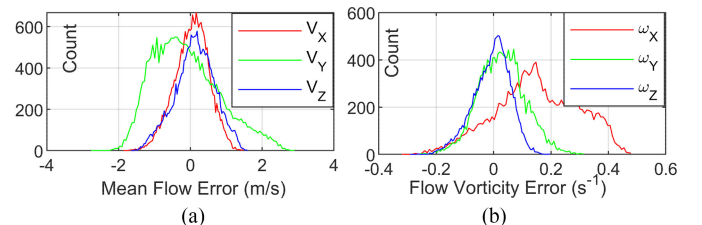


Fig. 12. Estimation error distribution. (a) Mean flow. (b) Flow vorticity.

shows histogram plots of the error distribution of the wind parameter estimates. Also, a significant variation in the error distribution was observed in the histogram plots. Mean error values for the mean-flow estimates were estimated to be $\{0.0372, -0.1091, 0.1188\}$ m/s along X , Y , and Z axes of the experimental setup's coordinate system. Similarly, the mean error for the vorticity estimates was estimated to be $\{0.1498, 0.0282, -0.0072\}$ per second. As the helicopter responds to the instantaneous wind conditions, and the turbulence is captured to be maximum in v_y and ω_x , the estimation errors are maximum in these parameters as well. However, these effects would be less prominent in open areas such as a ship flight deck. Not only is the predominant vortex shedding frequency of the air wake (0.544 Hz) better suited for the RC helicopter to respond to [16], lesser chances of rotor wakes and availability of free space for the helicopter to hover would allow for better separation of the turbulent and steady-state wind parameters.

VI. CONCLUSIONS AND FUTURE WORK

The paper demonstrated the use of novel dynamic modeling of an RC helicopter (with 30 states) for the estimation of ambient wind conditions (described by six parameters). In contrast to existing helicopter dynamic models, which only use single directional steady-state ambient vector, the proposed modeling technique models spatial variation in the ambient wind condition by incorporating local wind vorticity. Being able to estimate instantaneous wind parameters, the proposed system offers a safe and low-cost platform for the testing of control strategies for autonomous operations of helicopters in turbulent environments for both military and civilian applications.

Despite excellent modeling results during the model optimization procedure, some discontinuities were observed in the estimated wind patterns primarily because of rotor wakes and the exclusion of turbulent quantities are the estimations of the ground-truth wind map. The system could have performed better in larger test facilities (with controlled wind) enabling the helicopter to hover safely for longer durations. This could have enabled extraction and validation of the turbulent and steady-state wind parameters separately. In future work, approximate analytical rotor wake models will be explored along with including power plant and actuator models to provide a better characterization of the wind condition and helicopter dynamics. Furthermore, air wake model based helicopter control strategies will be explored for the development of autonomous wind mapping systems.

ACKNOWLEDGMENT

The authors would like to acknowledge the assistance from L. Karlin from VT athletics department for his help in facilitating indoor flight experiments. The authors are also thankful to Virginia Tech graduate students A. Williams, H. Ren, V. Kamidi, and B. Sebastian for their help in data collection and CFD studies.

REFERENCES

- [1] *Helicopter operating procedures for air-capable ships NATOPS manual*, US Naval Air Systems (NAVAIR) Command, Patuxent River, MD, USA, 2003.
- [2] B. Ferrier, J. Duncan, J. Nelson, D. Carico, D. Ludwig, and C. Deck, "Further validation of simulated dynamic interface testing techniques as a tool in the forecasting of air vehicle deck limits," in *Proc. ASNE Launch Recovery Symp.*, Alexandria, VA, Dec. 2010, pp. 115–133.
- [3] S. Polsky, R. Imber, R. Czerwiec, and T. Ghee, "A Computational and experimental determination of the air flow around the landing deck of a US navy destroyer (DDG): Part II," in *Proc. 37th AIAA Fluid Dyn. Conf. Exhibit*, Jun. 2007, pp. 1–12.
- [4] D. Lee, J. Horn, N. Sezer-Uzol, and L. Long, "Simulation of pilot control activity during helicopter shipboard operations," in *Proc. AIAA Atmospheric Flight Mech. Conf. Exhibit*, 2003, pp. 1–11.
- [5] J. Lusardi, *Control Equivalent Turbulence Input Model for the UH-60 Helicopter*. Davis, CA, USA: Univ. California, 2004.
- [6] T. D. Ngo and C. Sultan, "Model predictive control for helicopter shipboard operations in the ship airwakes," *J. Guid. Control. Dyn.*, vol. 39, no. 3, pp. 574–589, Mar. 2016.
- [7] T. Oktay and C. Sultan, "Constrained predictive control of helicopters," *Aircr. Eng. Aerosp. Technol.*, vol. 85, pp. 32–47, 2013.
- [8] T. Oktay, *Constrained Control of Complex Helicopter Models*. Blacksburg, VA, USA: Polytechnic State Univ., 2012.
- [9] P. P. Neumann and M. Bartholmai, "Real-time wind estimation on a micro unmanned aerial vehicle using its inertial measurement unit," *Sensors Actuators, A Phys.*, vol. 235, pp. 300–310, 2015.
- [10] R. Bardera and J. Meseguer, "Flow in the near air wake of a modified frigate," *Proc. Inst. Mech. Eng. G. J. Aerosp. Eng.*, vol. 229, no. 6, pp. 1003–1012, 2015.
- [11] M. R. Snyder, A. Kumar, P. Ben-Tzvi, and H. S. Kang, "Validation of computational ship air wakes for a naval research vessel," in *Proc. 51st AIAA Aerosp. Sci. Meeting*, Jan. 2013, pp. 1–25.
- [12] M. R. Snyder *et al.*, "USNA ship air wake program overview," in *Proc. 29th AIAA Appl. Aerodynamics Conf.*, Jun. 2011, pp. 1–12.
- [13] M. R. Snyder, H. S. Kang, C. J. Brownell, and J. S. Burks, "Validation of ship air wake simulations and investigation of ship air wake impact on rotary wing aircraft," in *Proc. Am. Soc. Nav. Eng. Launch Recover. Symp.*, 2012, p. 18.
- [14] C. J. Mallon *et al.*, "Measurements of ship air wake using airborne anemometers," in *Proc. 55th AIAA Aerosp. Sci. Meeting*, Jan. 2017, pp. 1–12.
- [15] K. Gamagedara, K. Patil, T. Lee, and M. R. Snyder, "Vision-based relative localization for airborne measurements of ship air wake," in *Proc. AIAA Atmos. Flight Mech. Conf.*, Jan. 2018, pp. 1–15.
- [16] A. Kumar, "Estimation and mapping of ship air wakes using RC helicopters as a sensing platform," Ph.D. dissertation Dept. Mech. Eng., Virginia Tech, Blacksburg, VA, USA, Apr. 2018.
- [17] J. Gonzalez-Rocha, C. A. Woolsey, C. Sultan, S. de Wekker, and N. Rose, "Measuring atmospheric winds from quadrotor motion," in *Proc. AIAA Atmospheric Flight Mech. Conf.*, Jan. 2017, pp. 1–22.
- [18] D. Phelps, K. Gamagedara, J. Waldron, K. Patil, and M. Snyder, "Ship air wake detection using small fixed wing unmanned aerial vehicle," in *Proc. AIAA Aerosp. Sci. Meet.*, Jan. 2018, pp. 1–11.
- [19] J. D. Metzger, "Measurement of ship air wake impact on a remotely piloted aerial vehicle," US Naval Academy, Annapolis, MD, USA, Project Rep., Sep. 2012.
- [20] A. Kumar and P. Ben-Tzvi, "Extraction of impact of wind turbulence on RC helicopters using machine learning," in *Proc. ASME Int. Des. Eng. Tech. Conf.*, 2016, pp. 1–7.
- [21] M. R. Snyder, A. Kumar, and P. Ben-Tzvi, "Off ship measurement of ship air wakes using instrumented unmanned aerial vehicles," in *Proc. AIAA Appl. Aerodynamics Conf.*, Jun. 2014, pp. 1–9.
- [22] A. Kumar, P. Ben-Tzvi, M. R. Snyder, and W. Saab, "Instrumentation system for ship air wake measurement," in *Proc. ROSE IEEE Int. Symp. Robot. Sensors Environ.*, 2013, Code 351, pp. 118–123.
- [23] A. Kumar and P. Ben-Tzvi, "Novel wireless sensing platform for experimental mapping and validation of ship air wake," *Mechatronics*, vol. 52, pp. 58–69, Apr. 2018.
- [24] R. T. N. Chen, "A survey of nonuniform inflow models for rotorcraft flight dynamics and control applications," *NASA Tech. Memo.*, vol. 14, no. 2, pp. 147–184, 1990.

- [25] G. D. Padfield, *Helicopter Flight Dynamics: The Theory and Application of Flying Qualities and Simulation Modelling*, 2nd ed. Oxford, U.K.: Blackwell Publishing, 2007.
- [26] R. Cunha and C. Silvestre, "Dynamic modeling and stability analysis of model-scale helicopters with bell-hiller stabilizing bar," in *Proc. AIAA Guid. Navig. Control Conf. Exhib.*, Aug. 2003, pp. 1–11.
- [27] A. Kumar and P. Ben-Tzvi, "An inertial sensor to measure wind turbulence with RC helicopters," in *Proc. ASME Dyn. Syst. Control Conf.*, 2017, pp. 2–7.
- [28] D. A. Spera, "Models of lift and drag coefficients of stalled and unstalled airfoils in wind turbines and wind tunnels," *NASA Glenn Research Center*, Cleveland, OH, USA, Contractor Rep., Oct. 2008, pp. 1–35.
- [29] J. A. Demoss, *Drag Measurements on an Ellipsoidal Body*. Blacksburg, VA, USA: Polytechnic Institute State University, 2007.
- [30] A. Kumar and P. Ben-Tzvi, "Spatial object tracking system based on linear optical sensor arrays," *IEEE Sens. J.*, vol. 16, no. 22, pp. 7933–7940, Nov. 2016.
- [31] P. Ben-Tzvi and A. Kumar, "Linear optical sensor arrays (LOSA) tracking system for active marker based 3D motion tracking," U.S. Patent US10295651B2, May 21, 2019.
- [32] M. Clerc and J. Kennedy, "The particle swarm-explosion, stability, and convergence in a multidimensional complex space," *IEEE Trans. Evol. Comput.*, vol. 6, no. 1, pp. 58–73, Feb. 2002.
- [33] "R. M. Young Company Ultrasonic Anemometer - Model 81000," 2004. [Online]. Available: <http://www.youngusa.com/products/6/3.html>. Accessed: Sep 16, 2016.
- [34] M. S. Arulampalam, S. Maskell, N. Gordon, and T. Clapp, "A tutorial on particle filters for online nonlinear/non-Gaussian Bayesian tracking," *IEEE Trans. Signal Process.*, vol. 50, no. 2, pp. 723–737, Feb. 2002.
- [35] S. Thrun, "Particle filters in robotics," in *Proc. Uncertainty AI*, Edmonton, AB, Canada, Aug. 2002, pp. 511–518.
- [36] P. M. Djuric *et al.*, "Particle filtering," *IEEE Signal Process. Mag.*, vol. 20, no. 5, pp. 19–38, Sep. 2003.



Pinhas Ben-Tzvi (S'02–M'08–SM'12) received the B.S. degree (*summa cum laude*) in mechanical engineering from the Technion—Israel Institute of Technology, Haifa, Israel, in 2000 and the M.S. and Ph.D. degrees in mechanical engineering from the University of Toronto, Toronto, ON, Canada, in 2004 and 2008, respectively.

He is currently an Associate Professor of Mechanical Engineering and Electrical and Computer Engineering, and the founding Director of the Robotics and Mechatronics Laboratory at Virginia Tech, Blacksburg, VA, USA. His current research interests include robotics and intelligent autonomous systems, human–robot interactions, robotic vision and visual servoing/odometry, machine learning, mechatronics design, systems dynamics and control, mechanism design and system integration, and novel sensing and actuation.

Dr. Ben-Tzvi was the recipient of the 2019 Virginia Tech Excellence in Teaching Award, 2018 Virginia Tech Faculty Fellow Award, the 2013 George Washington University, the School of Engineering and Applied Science (GWU SEAS) Outstanding Young Researcher Award and the GWU SEAS Outstanding Young Teacher Award, as well as several other honors and awards. He is a Technical Editor for the *IEEE/ASME Transactions on Mechatronics*, Associate Editor for *ASME Journal of Mechanisms and Robotics*, Associate Editor for *IEEE ROBOTICS AND AUTOMATION MAGAZINE*, and an Associate Editor for the *International Journal of Control, Automation and Systems*, and served as an Associate Editor for *IEEE ICRA* 2013, 2014, 2016, 2017, and 2018. He is a member of the American Society of Mechanical Engineers (ASME).



Anil Kumar (S'15–M'18) received the B. Tech Degree in electrical engineering from the Indian Institute of Technology (IIT), Roorkee, India, in 2010 and the Ph.D. degree in mechanical engineering from Virginia Tech, Blacksburg, USA, in 2018, under the supervision of Prof. Ben-Tzvi.

He was with the Biomedical Instrumentation Lab, IIT Roorkee, as a Research Fellow. He was with the Robotics and Mechatronics Laboratory, Virginia Tech, Blacksburg, USA, as a Graduate Researcher. He is currently working as a Senior

Engineer with GM Cruise, San Francisco, CA, USA. His research interests include optoelectronics, machine learning, computer vision, mechatronics design, signal and image processing, autonomous robotics, and instrumentation design.